Research Square

Preprints are preliminary reports that have not undergone peer review.
They should not be considered conclusive, used to inform clinical practice,
or referenced by the media as validated information.

RGB Image-based Retrieval of Extinction Coefficients and Ångström Exponent for Fog Characterization

Juhyeon Sim
Pukyung National University
Juseon Shin
Pukyung National University
Yunki Mun
Pukyung National University
Dukhyeon Kim
Hanbat National University
Youngmin Noh
nym@pknu.ac.kr

Pukyung National University

Research Article

Keywords:

Posted Date: April 27th, 2026

DOI: https://doi.org/10.21203/rs.3.rs-9273114/v1

License: This work is licensed under a Creative Commons Attribution 4.0 International License.
Read Full License

Additional Declarations: No competing interests reported.

Abstract

Fog is a meteorological phenomenon that significantly impacts traffic safety and public health. However, real-time monitoring remains challenging due to the spatially sparse distribution of dedicated observation networks. This is particularly problematic given the highly localized nature of fog formation. This study proposes an RGB image-based method to derive fog optical properties—specifically the extinction coefficient at three visible wavelengths (R:597nm, G:534nm, B:459nm) and the Ångström exponent (AE)— from pixel intensity differences of objects located at known distances. To support the observational analysis, we simulated extinction coefficients and AE based on a modified gamma distribution as a fog size distribution model. Simulation results showed that as fog particle size increases, the AE decreases toward zero or negative values. This is accompanied by an inversion of the wavelength-dependent extinction coefficient, where scattering at longer (red) wavelengths exceeds that at shorter (blue) wavelengths. These theoretical findings were consistent with observations from six fog events captured at 2-minute intervals during each event, between December 2021 and March 2023 in Daejeon, South Korea. When fog was present, the extinction coefficient increased and AE approached zero or negative values. Fog dissipation was marked by decreasing extinction coefficients and a recovery of AE toward positive values. An R/B extinction coefficient ratio greater than 1 was identified as a generally reliable indicator of fog presence. Direct RGB images based optical observations confirmed these findings across all six fog events. This approach offers a cost-effective and scalable alternative for fog monitoring using widely available imaging sources such as CCTVs.

1 Introduction

Fog is defined as the occurrence in which water droplets suspended near the surface of the Earth reduce horizontal visibility to below 1 km (Greer, 1996; Jarraud, 2008). Fog has complex formation and dissipation mechanisms and is highly localized in nature (Price et al., 2018; Hůnová et al., 2021). Many countries have established meteorological observation networks to monitor fog-related visibility reduction. South Korea operates 105 synoptic weather stations to observe visibility and fog occurrence (KMA, 2026). The United States runs approximately 900 stations under the Automated Surface Observing System (NOAA, 2026). Japan monitors visibility at approximately 155 manned and unmanned weather stations (JMA, 2026). However, these ground-based sensors only acquire localized air samples and nay mot be representative of the total areal extent of fog (David et al., 2015). The observation network is not dense enough to monitor the spatially heterogeneous nature of fog, and visibility sensors are costly to deploy (Xiao et al., 2023). Given that fog changes rapidly and exhibits localized characteristics, data from such sparse networks have limited practical value (Kulkarni et al., 2019).

Various instruments exist to measure the aerosol optical properties and concentration, a common limitation is their high cost. This restricts the number of observation sites and limits spatial resolution. Satellite-based approaches using MODIS and similar instruments have been explored, but have difficulty capturing the rapid changes in fog generation and dissipation. Numerical weather prediction (NWP) models have been used to forecast fog, but require accurate aerosol concentrations and fog droplet

number density as inputs, which are difficult to observe in practice (Boutle et al., 2018). Vehicle-mounted cameras have also been applied, but are limited to scenarios where only a road and sky are visible, making them unsuitable for dense urban environments (Hautiere et al., 2006). Low-cost sensors have been proposed as an alternative, but suffer from low measurement accuracy and difficulties in maintaining spatial coverage across large areas.

A promising solution is to derive aerosol optical properties from RGB images obtained by commercial cameras or CCTVs. Previous studies have shown that extinction coefficients at three wavelengths can be retrieved from pixel intensity differences between objects at known distances in landscape images (Park and Kim, 2020; Shin et al., 2022).

In this study, the Ångström exponent (AE), which provides information on particle size, was derived alongside the extinction coefficient. This enables characterization of fog particle size, going beyond the single-channel visibility estimation of conventional methods. Furthermore, a modified gamma distribution simulation was conducted to examine changes in AE and the wavelength-dependent inversion of the extinction coefficient during fog dissipation. Both AE and the R/B extinction coefficient ratio were evaluated as indicators of fog presence. While AE provides a quantitative measure of particle size derived from all three wavelengths, the R/B ratio offers a simpler, threshold-base criterion that does not require regression analysis, making it more suitable for real-time fog detection. This study extends the image-based extinction retrieval approach by incorporating AE as a particle size indicator, providing a means to distinguish fog-induced visibility reduction from pollution-driven degradation using widely available camera image. Given the rapid and localized mature of fog, this approach can be deployed across multiple sites simultaneously using widely available cameras such as CCTVs, enabling spatially dense and temporally continuous monitoring that conventional sparse networks cannot achieve.

2 Methodology and data

2.1 Extinction coefficient retrieval from image analysis

To retrieve atmospheric extinction coefficient, we analyzed images acquired from a commercially available digital camera (NIKON D7500). All images were captured under fixed settings: exposure time of 1/80 s, ISO 100, and aperture of f/4.5. An 18 mm lens was used, and a polarizing filter was placed in front of the lens to remove reflected light. Under daylight conditions, the sun was assumed to provide uniform illumination across all target objects. Images were captured at 2-minute intervals using the automatic interval shooting software provided by NIKON and saved in JPG format.

The extinction coefficient, which represents the amount of light attenuated per unit path length, is derived from the pixel intensity of the image. Pixel intensity is determined by various parameters including the reflectivity of the target object, atmospheric transmittance, and the extinction, scattering, and absorption of light in the atmosphere (Eq. 1).

$$i_{pixel}^{m}(\lambda) = C_1(\lambda)\exp(-\alpha r_m) + C_2(\lambda)\{1-\exp(-\alpha r_m)\}$$ Eq. 1

The first term in Eq. 1 represents the extinction of the target object itself, while the second term represents the integral of diffused light due to aerosols between the camera and the target objects. C_1 and C_2 are wavelength–dependent constants. C_1 represent the intrinsic radiance of the target object, and C_2 represents the background sky radiance determined by the aerosol scattering phase function. The effective wavelengths used for the RGB channels are 597, 534, and 459 nm, respectively. These were determined by accounting for the solar spectral intensity, sensor sensitivity, and the frequency of extinction at each wavelength. For more information, see Shin et al. (2022).

For m target objects (T_m), r_m denotes the distance to T_m in meters, and α denotes the extinction coefficient (m^{-1}). This equation can be applied when objects with similar reflective properties exist at different distances within the image, and when the pixel intensity I and the distance to each target are known. Among the pixels within each target region, the minimum pixel value was selected for analysis. This approach reduces the influence of direct surface reflectance on the retrieved signal, thereby improving sensitivity to atmospheric optical properties.

Images were acquired from a camera installed at a residential building in Gwanpyeong-dong, Daejeon, South Korea (36.42°N, 127.39°E, ~ 36 m a.g.l.). Apartment building entrances located at similar viewing angles and with comparable reflective properties were selected as target objects (Fig. 1a). The observation site is frequently affected by fog due to the nearby Gapcheon River (drainage area: 649 km^2) to the northeast.

Four target objects and sky pixel were used to obtain five equations from Eq. 1. The RGB intensity values as a function of target distance were fitted using an exponential function, with the exponent term yielding the extinction coefficient (Fig. 1b). Initial values for the variables in Eq. 1 were set using the minimum pixel values for C_1 and maximum pixel values for C_2 across each RGB channel. Optimization was performed by minimizing the sum of squared errors between the measured and calculated values.

In urban fog, the extinction coefficient is dominated by scattering rather than absorption(Chen et al., 2024) ,and is more strongly influenced by near-field visibility than long-range visibility. When visibility is poor, signals from distant targets become saturated. To capture near-field fog particles, targets within 300 m were used, and the sky distance was set to 1 km. The distances to targets T1 through T4 are 50 m, 107 m, 184 m, and 269 m, respectively. The effective wavelengths were determined by considering the spectral intensity of sunlight, sensor sensitivity, and the extinction coefficient frequency at each wavelength (Park and Kim, 2020; Kim and Noh, 2021; Shin et al., 2022).

To examine changes in particle size during fog growth, we derived AE, calculated from the ratio of extinction coefficients at two wavelengths (Schuster et al., 2006; Kaskaoutis et al., 2007). In general, AE decreases as the proportion of larger particles increases, and increases as smaller particles dominate (Pinnick et al., 1979; Schuster et al., 2006). Since extinction coefficients were derived at three

wavelengths in the visible range, AE was calculated by applying a linear regression to the logarithmic ratios of extinction coefficients at all three wavelengths.

$$XP_1 = ln\lambda_R - ln\lambda_R,\ \ XP_2 = ln\lambda_G - ln\lambda_R,\ \ XP_3 = ln\lambda_B - ln\lambda_R \text{ Eq. (2)}$$

$$YP_1 = ln\alpha_R - ln\alpha_R,\ \ YP_2 = ln\alpha_G - ln\alpha_R,\ \ YP_3 = ln\alpha_B - ln\alpha_R \text{ Eq. (3)}$$

The logarithmic ratios for each wavelength (R,G,and B) were first computed to define the coordinates XP and YP (Equations 2 and 3). A linear regression fit was then applied to these coordinate values. The slope of the fitted line was used as the AE, serving as an indicator of particle size.

2.2 Fog simulation

To examine the change in the extinction coefficient and AE caused by fog particles, we calculated theoretical extinction coefficients (α) based on an assumed fog number size distribution $(N(r))$, using the extinction efficiency (Q) at RGB effective wavelengths.

$$\alpha\ (\lambda) = \int_0^\infty \pi\, r^2 Q\,(\lambda, r, m)\, N\,(r)\, dr \text{ Eq. (4)}$$

Here, r is the aerosol radius (as μm), m is the refractive index, and λ represents the effective wavelength (R: 597 nm, G: 534 nm, and B: 459 nm). The extinction coefficient is calculated by integrating the product of the extinction efficiency and the aerosol surface distribution $\left(\pi\, r^2 N\,(r)\right)$ over all particle sizes.

The fog droplet size distribution was modelled using a modified gamma distribution, which has been widely used in previous research to describe aerosol number size distribution of non-uniform and irregular particles such as fog and cloud droplets (Deirmendjian, 1969; Tomasi et al., 1975; Hess et al., 1998; Vivekanandan et al., 1999; Lu et al., 2020). The modified gamma distribution was selected over bimodal distributions because fog droplet populations are predominantly governed by condensational growth during the formation phase, producing a unimodal size distribution (Mazoyer et al., 2022). Bimodal distributions, which assume distinct fine and coarse modes, are more representative of general atmospheric aerosols than of fog droplets (Schuster et al., 2006). The modified gamma distribution is determined by four positive parameters and can be described by the following Eq. 5 (Deirmendjian, 1969).

$$\backslash\text{raisebox}1ex\$dN\$/\backslash\text{raisebox}{-}1ex\$dr\$ = Nar^\alpha \exp\left[-\frac{\alpha}{\gamma}\left(\frac{r}{r_c}\right)^\gamma\right],\ \ 0 \le\ r < \infty \text{ Eq. (5)}$$

In $\backslash\text{raisebox}1ex\$dN\$/\backslash\text{raisebox}{-}1ex\$dr\$$, N represents the total number density (in particles per cubic centimetres, cm^{-3}). The parameter α and γ determine the slope of the size distribution, while a is a normalization constant that converts the total number density to a value calculated from the integral over the entire particle size range. r_c denotes the mode radius (in μ m), which is the most frequent particle size and is associated with particle growth.

This study set the size range of fog droplet from 0.001 to 10 μ m, and the variation of r_c from 0.001 to 5 μ m. The parameters α and γ vary across studies depending on the aerosol or fog type considered (Deirmendjian, 1969; Tampieri and Tomasi, 1976; Hess et al., 1998; Vivekanandan et al., 1999; Lu et al., 2020). The fog model of the optical properties of Aerosol and Clouds (OPAC) software, which can simulate the optical properties of cloud and mixed aerosol particles, sets α and γ to 4 and 1.77, respectively (Hess et al., 1998). In contrast, a study simulating the modified gamma distribution parameters according to the type of fog (i.e., radiation fog, ground fog, etc.) used different parameters for each type (Tampieri and Tomasi, 1976). We referred to the parameter ranges set in the latter study and varied α and γ from 1 to 6 to observe the changes. When either α or γ was varied individually, the fixed values of the remaining variables were set to 4 and 1.77, respectively, as in OPAC. Using 100 random parameters, we calculated the number size distribution and the extinction efficiency of fog particles at known wavelengths. From these, we derived the extinction coefficients and AE using the method described in Section 2.1.

3. Results and discussion

We observed six fog events over approximately 16 months, from December 8, 2021 to March 23, 2023, with images captured continuously at 2-minute intervals. Particle properties and meteorological conditions were analyzed, including mass concentration, extinction coefficient, AE, and relative humidity. Simulation results based on the modified gamma distribution are present in Section 3.3 to provide a theoretical basis for interpreting the observed AE behavior under fog and non-fog conditions.

3.1 Temporal variations in RGB inversion and AE

Figure 3 presents the observational results from sunrise through complete fog dissipation on November 2, 2022. Figure 3(a) shows the time series of extinction coefficients at each wavelength and the R/B ratio. The AE derived from the extinction coefficients is shown in Fig. 3(b). The PM mass concentrations in Fig. 3(c) were obtained from a national air quality monitoring station (AirKorea) located 800 m northeast of the observation site. The relative humidity at 1-minute intervals and visibility at 1-hour intervals in Fig. 3(d) were obtained from the Automated Synoptic Observing System (ASOS) Daejeon station, located 5.4 km southwest of the observation site.

While fog was present, Fig. 3(a) shows that the extinction coefficient at the longer red wavelength was equal to or greater than that at the shorter blue wavelength. This is more clearly confirmed in the AE plot (Fig. 3(b)). As fog particles grow, forward scattering intensifies at all wavelengths, and the AE approaches a near-zero or negative value. Around 9 AM, as the fog dissipated, the AE increased to a positive value close to 1, confirming fog dissipation based on solely on the optical retrieval. The camera images also confirm that ground fog dissipated and visibility was restored between 8:33 AM and 8:41 AM.

Under non–fog conditions, scattering is stronger at the blue wavelength due to wavelength-dependent differences, consistent with Mie theory. However, as fog particles grow beyond the size of all visible wavelengths, wavelength dependence decreases and the scattering at red and blue wavelengths becomes comparable, resulting in inversion. The sharp decrease in extinction coefficient observed between 8 and 9 AM, during fog dissipation, is tentatively attributed to particle size passing through the first peak of the Mie extinction efficiency curve. Direct particle size measurements were not available in this study, so this interpretation remains speculative.

PM concentrations remained high regardless of fog presence, with PM_{10} and $PM_{2.5}$ averaging 57.2 and 37.6 μg/m³ respectively, and the $PM_{2.5}/PM_{10}$ ratio remained stable between 0.57 and 0.73. This provides additional evidence that the changes in Figs. 4(a) and 4(b) were caused by fog rather than fine particles. Relative humidity and visibility measured at the meteorological station showed differences before and after fog dissipation. From around 9 AM, relative humidity decreased and visibility began to exceed 3 km.

3.2 Comparison of extinction coefficient and AE between fog and non-fog periods

Six fog events were observed during the measurement period. Figure 4(a) shows the extinction coefficient and AE, and Fig. 4(b) shows relative humidity and $PM_{2.5}$ concentration, separated into fog and non-fog periods for each case. The extinction coefficient and AE were derived using the method described in Section 2.1. Relative humidity and $PM_{2.5}$ were obtained from ASOS and AirKorea respectively. Observation dates are distinguished by color, with fog presence indicated by open circles and post-dissipation by filled squares.

Despite differences in absolute values, all six cases showed lower AE and higher extinction coefficients during fog compared to non-fog periods in the same timeframe. This is consistent with the findings in Section 3.1 and agree with previous studies reporting that extinction coefficients increase at all wavelengths during fog but at different rates, and that AE decreases with increasing particle size (Pinnick et al., 1979; Schuster et al., 2006). However, the magnitude of these differences varied between cases. For example, Case 6 (March 23, 2023) showed an AE above 0.2 even during fog, unlike the other cases where AE was negative. However, the decrease in extinction coefficient and increase in AE during fog dissipation were similar to other cases. The difference in Case 6 is likely attributable to higher-than-usual PM concentrations on that day. The average PM_{10} and $PM_{2.5}$ concentrations during the image analysis period (08:00–15:00) were 69.4 and 63.0 μg/m³ respectively, with a $PM_{2.5}/PM_{10}$ ratio of approximately 0.91, indicating that most of the particulate mass was in fine form. This suggests that the increased extinction coefficient and reduced visibility on that day were influenced not only by fog but also by fine particles. The mixture of large fog particles and fine particles resulted in a higher AE than other fog events. The elevated $PM_{2.5}$ may also suggest a higher number concentration of fog condensation nuclei, potentially suppressing individual particle growth and preventing the mode radius from reaching the threshold required for wavelength-dependent inversion. In this case, the increased extinction coefficient would reflect higher number concentration rather than enhancement extinction

efficiency pre particle. However, this interpretation remains speculative without direct particle size measurements. $PM_{2.5}$ also remained elevated after fog dissipation ($PM_{2.5}$: 63.0 μg/m³, PM_{10}: 67 μg/m³ at 10 AM).

3.3 Simulation of extinction coefficient and AE for fog

As observed in Section 3.1, the AE approaches zero during fog events, owing to the decrease in wavelength-dependent scattering efficiency as fog particle grow. The observed near-zero or negative AE values during for presence are in agreement with the simulation results below. To support this interpretation, we used the modified gamma distribution, as described in Section 2.2 to simulated extinction coefficients and AE by fog formation(□□ □□□□ □□/□□ □□□ □□).

The parameters α and γ, which determine the slope of the MGD, were varied to analyse how the extinction coefficients at three wavelengths and the AE change as the mode radius increases. The mode radius represents the peak radius of the distribution. As the mode radius increases, the extinction coefficient undergoes wavelength-dependent inversion and the AE gradually decreases, converging toward zero when the radius reaches 0.5–1 μm (Fig. 5). Examining the extinction coefficient in more detail, a wavelength-dependent inversion occurs once the mode radius exceeds a certain threshold. This is because the difference in scattering efficiency across wavelengths decreases as fog particles grow larger. When fog particles grow sufficiently, the difference in scattering efficiency across wavelengths diminishes, leading to wavelength inversion.

Since AE is calculated from the ratio of extinction coefficients at different wavelengths (Equations 2 and 3), it converges toward zero as the difference between extinction coefficients decreases. This behaviour differs from that observed when general atmospheric aerosols composed solely of small particles increase. Under worsening air pollution, the fine particle fraction in the bimodal distribution of atmospheric aerosols increases, causing a stronger influence on extinction and raising the extinction coefficient. However, wavelength-dependent inversion of the extinction coefficient does not occur in this case. This distinction enables the method to differentiate fog-induced visibility reduction from pollution-driven degradation.

During foggy conditions, wavelength-dependent inversion between the red and blue wavelengths in the extinction coefficients was observed. As the fog disappeared, aerosol scattering caused the extinction coefficient measured at the blue wavelength to exceed that at the red wavelength. Using this observation, the ratio of the extinction coefficients at the red and blue wavelengths (R/B ratio) was used as a criterion for identifying fog presence. Specifically, a ratio greater than 1 indicated fog, while less than 1 indicated non-fog conditions.

Additionally, we simulated AE distribution under fog and non-fog conditions by varying α and γ of the MGD (Fig. 6). In the foggy state, the AE was close to zero due to the growth of fog particles. In the non-fog state, where scattering at the blue wavelength was equal to or greater than that at the red

wavelength, the AE increased. As fog particles became smaller and eventually disappear, the inversion of the R/B ratio ceases to occur.

4. Conclusion

This study demonstrated that RGB image-based retrieval of extinction coefficients and AE can effectively capture the optical signature of fog. During fog events, wavelength-dependent inversion of extinction coefficients and convergence of AE toward zero were consistently observed, in agreement with Mie scattering theory. As fog particles grow beyond the wavelength of visible light, scattering efficiency becomes less wavelength-dependent, reducing the spectral contrast that AE measures. This physical mechanism was reproduced in the modified gamma distribution simulations, supporting the validity of the proposed approach.

Across all six fog events, extinction coefficients were consistently higher and AE lower during fog compared to non-fog period. These results have agreement with previous in situ measurement of fog optical properties (Pinnick et al., 1979; Schuster et al., 2006). The R/B extinction coefficient ratio greater than 1 was identified as a reliable indicator of fog presence across five of the six observed cases. This threshold-based criterion offers a straightforward and computationally inexpensive means of fog detection that could be implemented in real-time monitoring systems. The exception, Case 6, occurred under unusually high fine particle concentrations ($PM_{2.5}/PM_{10}$ ratio of 0.91), where the competing effect of fine particles partially offset the AE reduction caused by for particle growth. This suggest that concurrent PM measurements should be considered as supplementary indicator in heavily polluted environments.

Previous image-based fog detection methods have primarily focused on visibility estimation from pixel brightness or contrast attenuation (Hautiere et al., 2006). The present approach goes beyond visibility estimation by retrieving wavelength-resolved optical properties, enabling characterization of particle size through AE. This represents a meaningful advance over single-channel brightness-based methods. Under increasing fine particle pollution, extinction coefficients rise but wavelength-dependent inversion does not occur, as fine particles remain small relative to visible wavelengths. This contrasts with fog conditions, where particle growth leads to spectral inversion and AE convergence toward zero. Such discrimination is not achievable with conventional single-wavelength visibility instruments. By incorporating AE alongside the extinction coefficient, the proposed approach enables characterization of aerosol particle size from camera image, representing a meaningful extension of pervious image-based methods that focused solely on extinction retrieval (Park and Kim, 2020; Kim and Noh, 2021; Shin et al., 2022).

The method has several limitations. First, it requires at least three target objects with known distances and similar reflective properties within the field of view on camera. This constrains deployment to structured environments such as urban areas and may limit applicability in open terrain, coastal zones, or forested areas. Furthermore, the present dataset is restricted to six fog events occurring at a single

urban location in Daejeon, South Korea. Although the consistency of the findings across these instances is promising, validation across a broader spectrum of diverse geographic contexts, fog types, and seasonal variations is essential to facilitate wider applicability. Thirdly, the study employed fixed camera settings throughout its duration, and fluctuations in illumination, including cloud cover or low sun angles, could potentially introduce uncertainty in the retrieval of pixel intensity. Consequently, future investigations should evaluate the method's sensitivity to these variables and investigate adaptive correction methodologies.

Despite these limitations, the proposed approach offers several practical advantages. Commercial cameras and CCTVs are widely deployed in transportation infrastructure, providing an existing observational network that could be leveraged for fog monitoring at minimal additional cost. The simultaneous retrieval of extinction coefficients at three wavelengths and AE from a single image frame enables both fog detection and particle size characterization, capabilities not available from conventional single-channel visibility sensors. These characteristics make the method well suited for real-time fog monitoring at high-risk locations such as airports and highway sections with frequent fog-related accidents. Given the rapid and localized nature of fog, the scalability of this approach across multiple CCTV sites offers a means to overcome the spatial limitations of conventional sparse observation networks.

Declarations

Code and data availability

The code and data used for the analysis in this study is available from the corresponding author upon request.

Competing interests

The authors declare that they have no competing interests.

Financial support

This research was supported by a grant (2023-MOIS-20024324) of Ministry-Cooperation R&D Program of Disaster-Safety funded by Ministry of Interior and Safety (MOIS, Korea).

Author Contribution

JSim and DK conceptualized the study and designed the methodology; DK and YM performed the data analysis; Jsim and DK developed the code; Jsim and DK wrote the original draft of the manuscript; JShin

and YN reviewed and edited the manuscript; and YN and DK supervised the study. All the authors discussed the results and approved the final manuscript.

Acknowledgement

This research was supported by a grant (2023-MOIS-20024324) of Ministry-Cooperation R&D Program of Disaster-Safety funded by Ministry of Interior and Safety (MOIS, Korea).

References

1. Boutle, I., Price, J., Kudzotsa, I., Kokkola, H. and Romakkaniemi, S. (2018). Aerosol–Fog Interaction and the Transition to Well-Mixed Radiation Fog. *Atmospheric Chemistry and Physics* 18: 7827–7840.
2. Chen, R., Zhang, Y., Xu, Q., Han, Y. and Wu, Z. (2024). Multiple Scattering of Bessel Beams Propagating in Advection Fog and Radiation Fog. *Frontiers in Physics* 12: 1356528.
3. David, N., Sendik, O., Messer, H. and Alpert, P. (2015). Cellular Network Infrastructure: The Future of Fog Monitoring? *Bulletin of the American Meteorological Society* 96: 1687–1698.
4. Deirmendjian, D. (1969). Electromagnetic Scattering on Spherical Polydispersions. *American Elsevier Publishing Company*.
5. Greer, I. (1996). Glossary of Meteorology. *Boston, MA: American Meteorological Society. Retrieved January* 11: 2009.
6. Hautiere, N., Tarel, J.-P., Lavenant, J. and Aubert, D. (2006). Automatic Fog Detection and Estimation of Visibility Distance through Use of an Onboard Camera. *Machine vision and applications* 17: 8–20.
7. Hess, M., Koepke, P. and Schult, I. (1998). Optical Properties of Aerosols and Clouds: The Software Package Opac. *Bulletin of the American meteorological society* 79: 831–844.
8. Hůnová, I., Brabec, M., Malý, M., Dumitrescu, A. and Geletič, J. (2021). Terrain and Its Effects on Fog Occurrence. *Science of the Total Environment* 768: 144359.
9. Jarraud, M. (2008). Guide to Meteorological Instruments and Methods of Observation (Wmo-No. 8). *World Meteorological Organisation: Geneva, Switzerland* 29.
10. JMA. Surface Observation, https://www.jma.go.jp/jma/en/Activities/surf/surf.html, Last Access: 2026.03.27.
11. Kaskaoutis, D., Kambezidis, H., Hatzianastassiou, N., Kosmopoulos, P. and Badarinath, K. (2007). Aerosol Climatology: Dependence of the Angstrom Exponent on Wavelength over Four Aeronet Sites. *Atmospheric chemistry and physics discussions* 7: 7347–7397.
12. Kim, D. and Noh, Y. (2021). An Aerosol Extinction Coefficient Retrieval Method and Characteristics Analysis of Landscape Images. *Sensors* 21: 7282.
13. KMA. Automated Synoptic Observing System (Asos), https://data.kma.go.kr, Last Access: 03/27.
14. Kulkarni, R., Jenamani, R.K., Pithani, P., Konwar, M., Nigam, N. and Ghude, S.D. (2019). Loss to Aviation Economy Due to Winter Fog in New Delhi during the Winter of 2011–2016. *Atmosphere* 10:

198.

15. Lu, C., Liu, Y., Yum, S.S., Chen, J., Zhu, L., Gao, S., Yin, Y., Jia, X. and Wang, Y. (2020). Reconciling Contrasting Relationships between Relative Dispersion and Volume-Mean Radius of Cloud Droplet Size Distributions. *Journal of Geophysical Research: Atmospheres* 125: e2019JD031868.
16. Mazoyer, M., Burnet, F. and Denjean, C. (2022). Experimental Study on the Evolution of Droplet Size Distribution during the Fog Life Cycle. *Atmospheric Chemistry and Physics* 22: 11305–11321.
17. NOAA. Automated Surface Observing Systems (Asos), https://www.ncei.noaa.gov/products/land-based-station/automated-surface-weather-observing-systems, Last Access:
18. Park, S. and Kim, D. (2020). Aerosol-Extinction Retrieval Method at Three Effective Rgb Wavelengths Using a Commercial Digital Camera. *Korean Journal of Optics and Photonics* 31: 71–80.
19. Pinnick, R., Jennings, S., Chýlek, P. and Auvermann, H. (1979). Verification of a Linear Relation between Ir Extinction, Absorption and Liquid Water Content of Fogs. *Journal of Atmospheric Sciences* 36: 1577–1586.
20. Price, J., Lane, S., Boutle, I., Smith, D., Bergot, T., Lac, C., Duconge, L., McGregor, J., Kerr-Munslow, A. and Pickering, M. (2018). Lanfex: A Field and Modeling Study to Improve Our Understanding and Forecasting of Radiation Fog. *Bulletin of the American Meteorological Society* 99: 2061–2077.
21. Schuster, G.L., Dubovik, O. and Holben, B.N. (2006). Angstrom Exponent and Bimodal Aerosol Size Distributions. *Journal of Geophysical Research: Atmospheres* 111.
22. Shin, J., Kim, D. and Noh, Y. (2022). Estimation of Aerosol Extinction Coefficient Using Camera Images and Application in Mass Extinction Efficiency Retrieval. *Remote Sensing* 14: 1224.
23. Tampieri, F. and Tomasi, C. (1976). Size Distribution Models of Fog and Cloud Droplets in Terms of the Modified Gamma Function. *Tellus* 28: 333–347.
24. Tomasi, C., Guzzi, R. and Vittori, O. (1975). The “So 2–Nh 3–Solution Droplets” System in an Urban Atmosphere. *Journal of Atmospheric Sciences* 32: 1580–1586.
25. Vivekanandan, J., Martner, B.E., Politovich, M.K. and Zhang, G. (1999). Retrieval of Atmospheric Liquid and Ice Characteristics Using Dual-Wavelength Radar Observations. *IEEE transactions on geoscience and remote sensing* 37: 2325–2334.
26. Xiao, P., Zhang, Z., Luo, X., Sun, J., Zhou, X., Yang, X. and Huang, L. (2023). Highway Visibility Estimation in Foggy Weather Via Multi-Scale Fusion Network. *Sensors* 23: 9739.

Figures

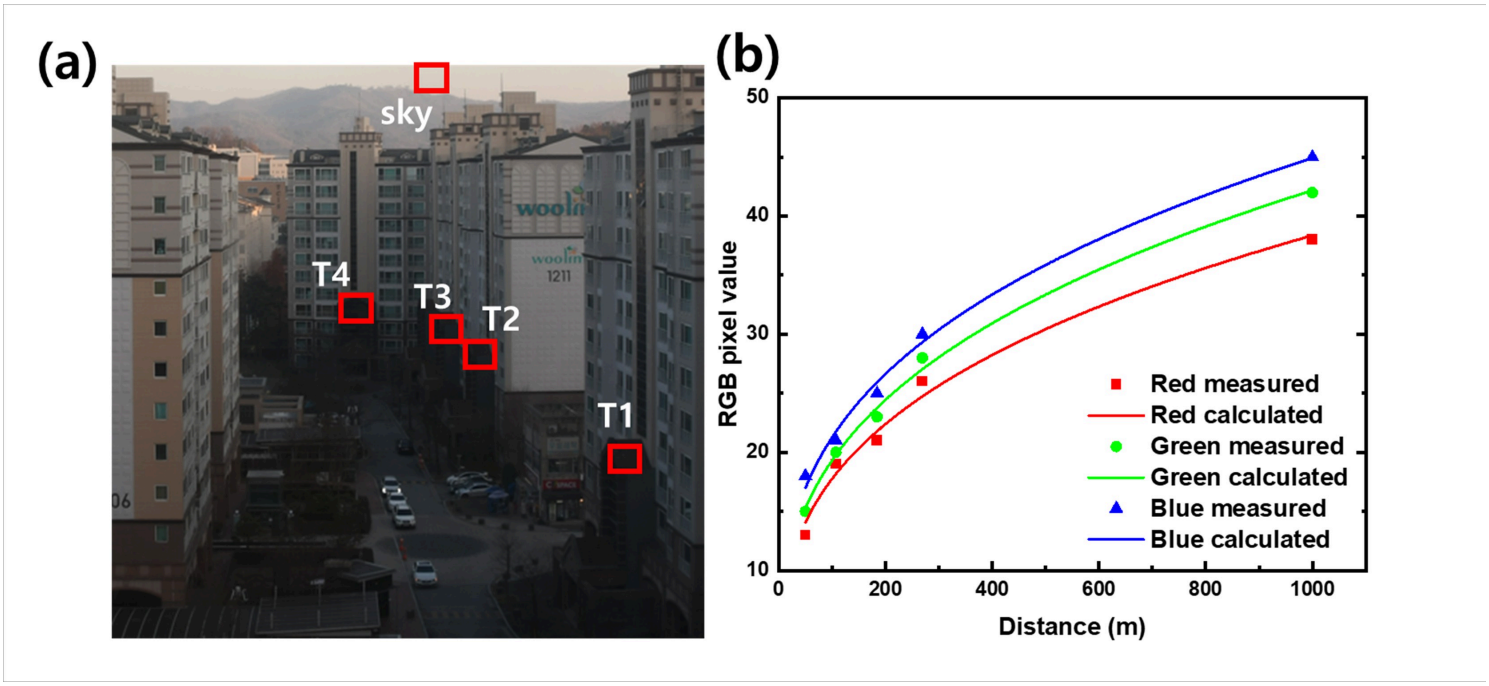


Figure 1

An example of pixel value extraction from targets located at different distances: (a) each target location in the image and (b) each target RGB signal fitting graph

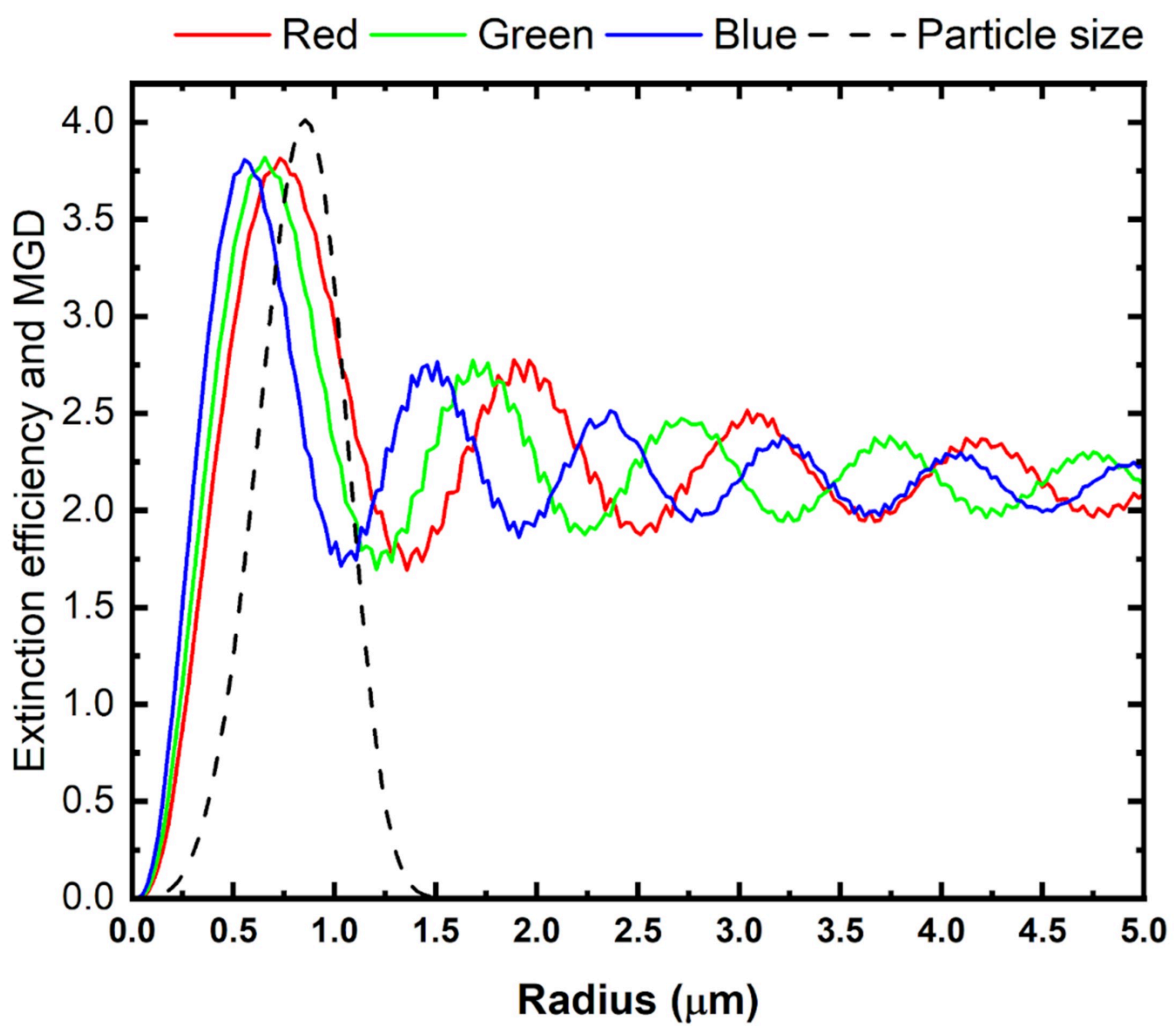
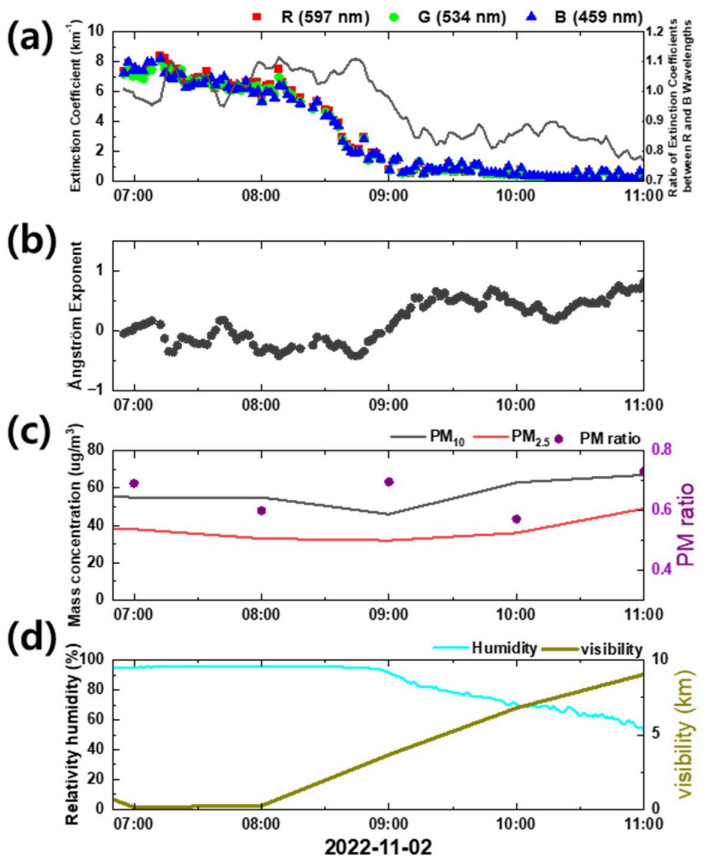


Figure 2

The number size distribution (#/cm^{-3}) of simulated fog droplet described by the modified gamma distribution (dotted line) and the extinction efficiency at the effective wavelengths of RGB channels (solid line)



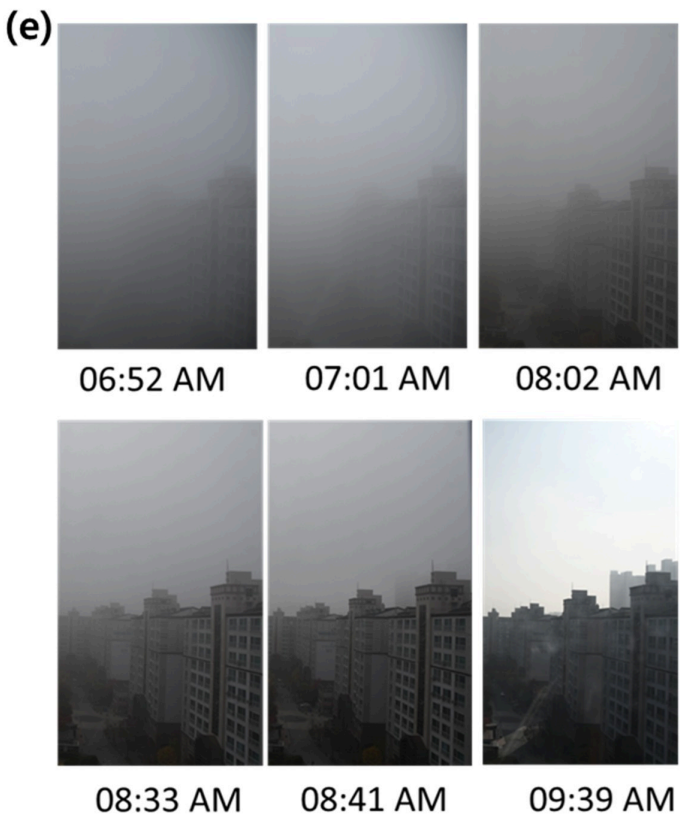


Figure 3

Temporal variations in (a) extinction coefficient and their ratio at three wavelengths; (b) AE; (c) particle mass concentration and their ratios; and (d) relative humidity (%) and visibility distance (km), and (e) camera images (November 2, 2022)

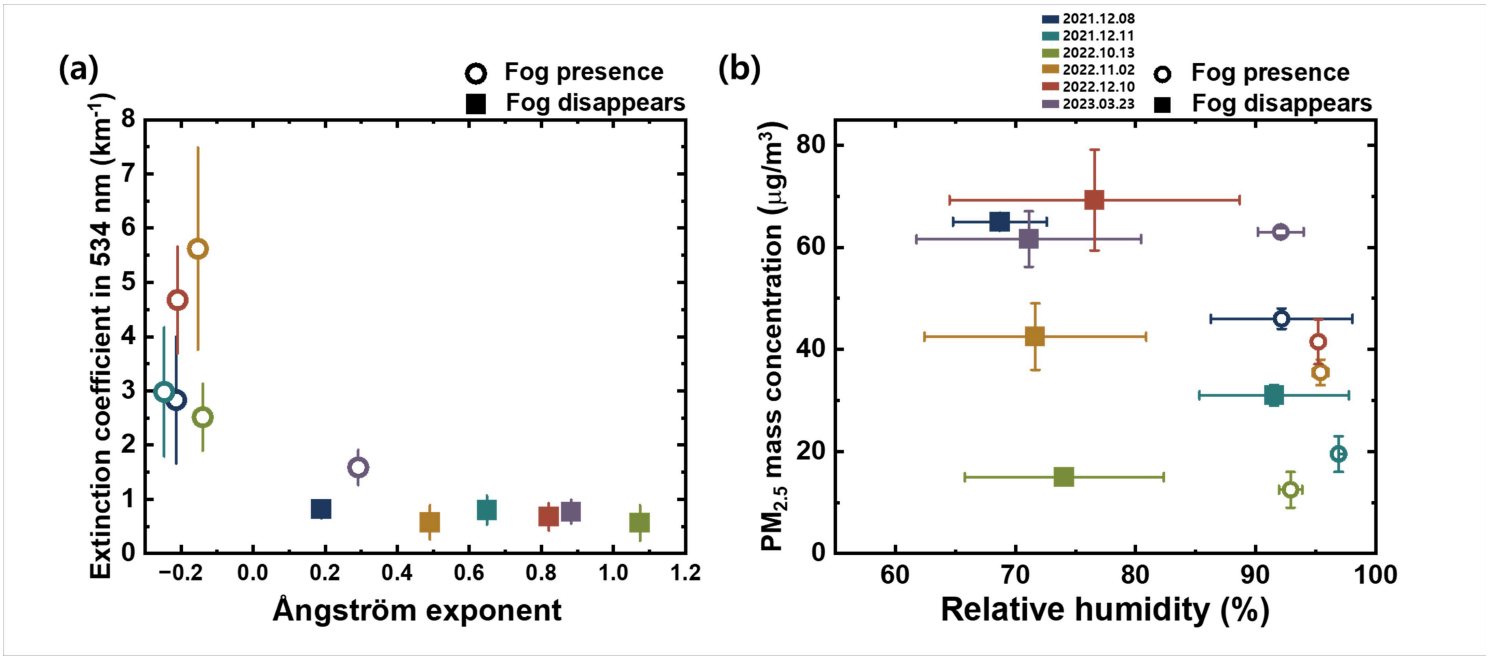


Figure 4

(a) Ångström exponent and extinction coefficient at G (534 nm) and (b) relative humidity and $PM_{2.5}$ mass concentration during the presence and dissipation of fog for each of the six fog cases

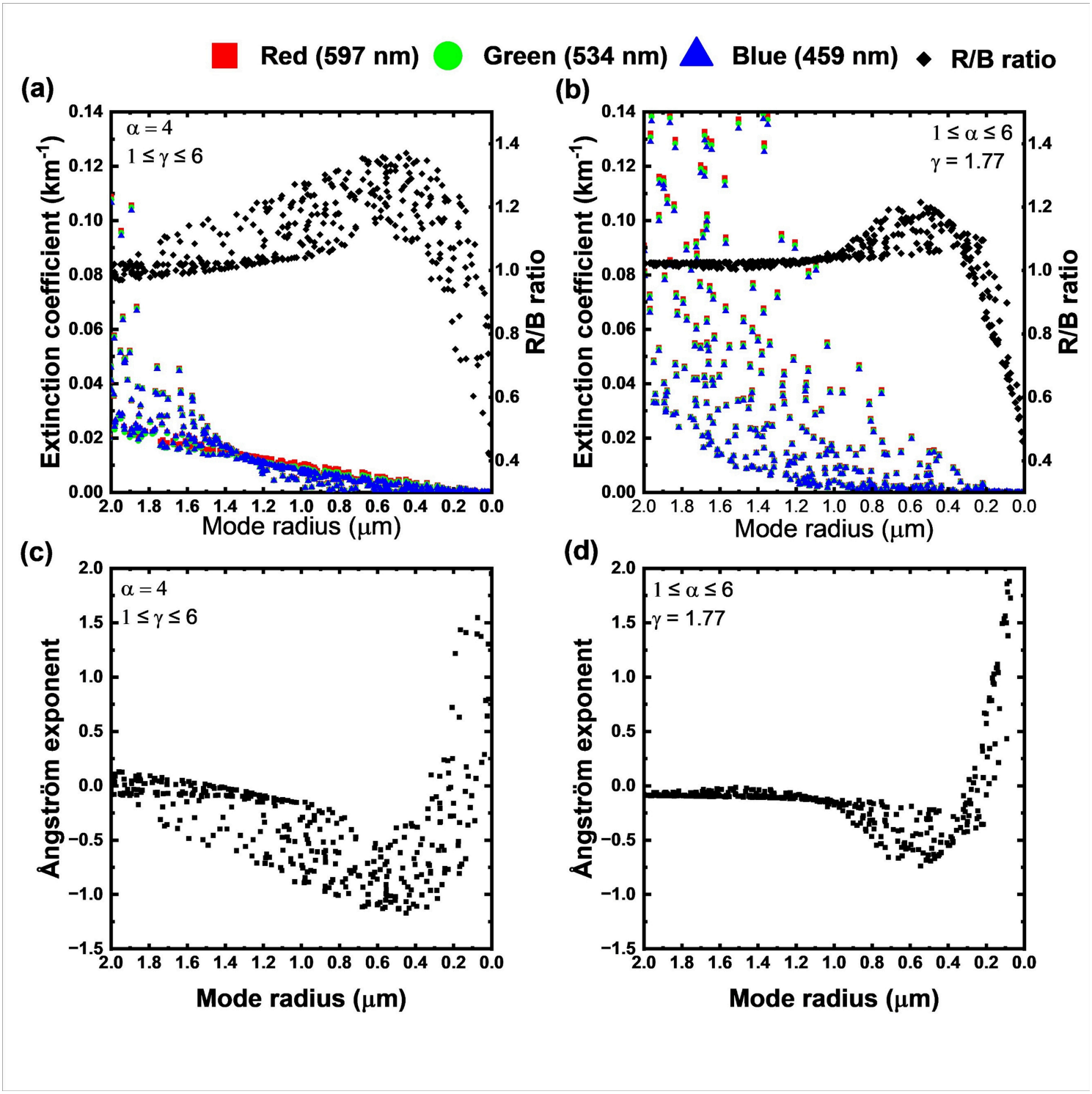


Figure 5

Simulated extinction coefficients and AE as a function of mode radius, with (a, c) γ fixed at 1.77 and (b, d) α fixed at 4.

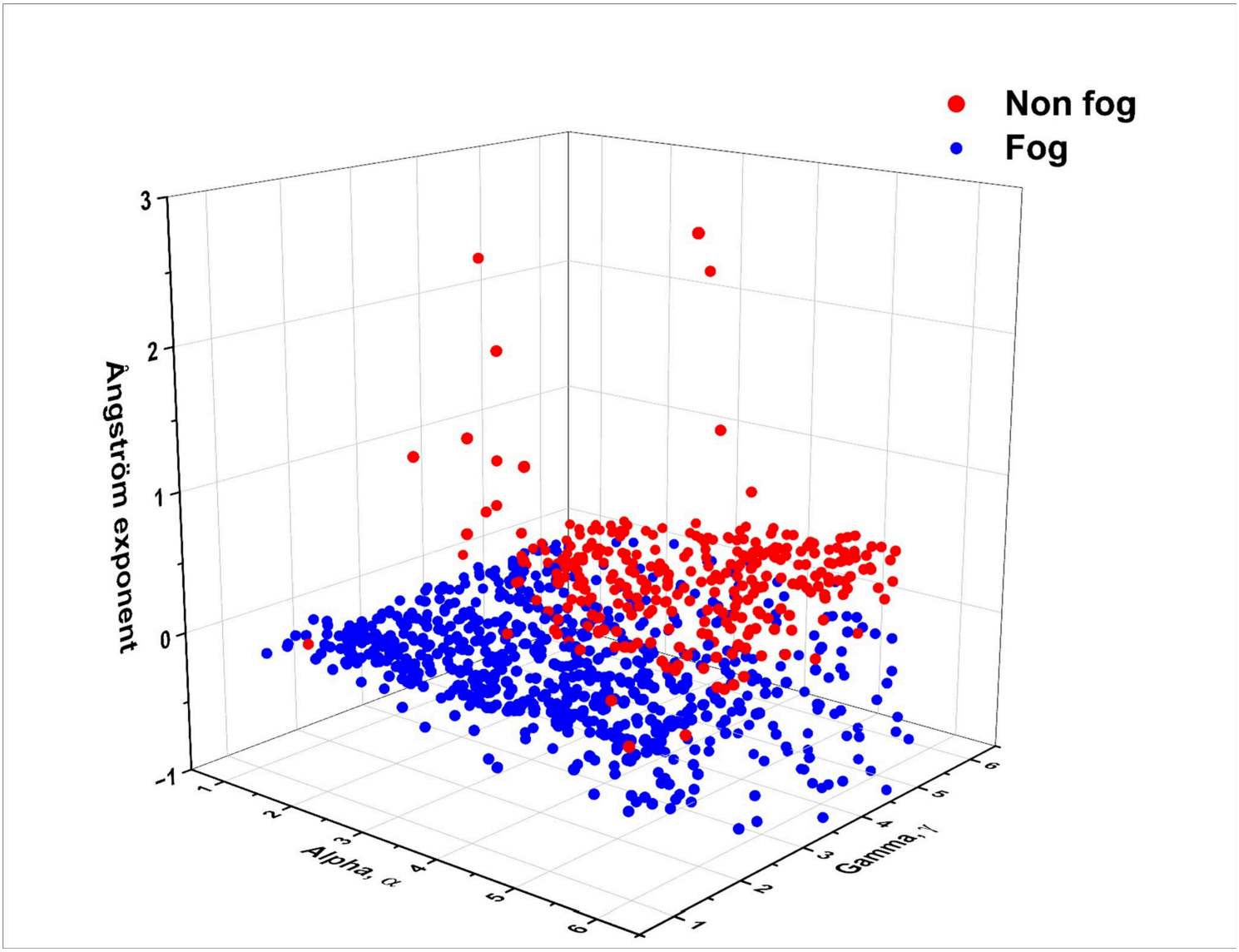


Figure 6

Distribution of AE values for fog and non-fog conditions as a function of alpha (α) and gamma (γ)